

# Experimental Study of Magnetically-Actuated Satellite Swarm: Controllability Extension via Time-Integrated Control with Geometry Learning

Yuta Takahashi

*Mechanical Engineering*

*Institute of Science Tokyo*

*Interstellar Technologies Inc.*

Tokyo, Japan

takahashi.y.cl@m.titech.ac.jp

Hideki Yoshikado

*Satellite Research and Development*

*Interstellar Technologies Inc.*

Tokyo, Japan

hideki.yoshikado@istellartech.com

Sumio Morioka

*Satellite Research and Development*

*Interstellar Technologies Inc.*

Tokyo, Japan

sumio.morioka@istellartech.com

Seang Shim

*Satellite Research and Development*

*Interstellar Technologies Inc.*

Tokyo, Japan

seang.shim@stellartech.com

Masaru Ishida

*Satellite Research and Development*

*Interstellar Technologies Inc.*

Tokyo, Japan

masaru.ishida@stellartech.com

Shin-Ichiro Sakai

*Spacecraft Engineering*

*Institute of Space and Astronautical Science*

Tokyo, Japan

sakai@isas.jaxa.jp

Yusuke Sawanishi

*Satellite Research and Development*

*Interstellar Technologies Inc.*

Tokyo, Japan

yusuke.sawanishi@stellartech.com

Noritsuna Imamura

*Our Stars*

*Interstellar Technologies Inc.*

Tokyo, Japan

noritsuna.imamura@stellartech.com

Takahiro Inagawa

*Satellite Research and Development*

*Interstellar Technologies Inc.*

Tokyo, Japan

takahiro.inagawa@stellartech.com

**Abstract**—This study aims to experimentally validate the principle of large-scale satellite swarm control using magnetic field interactions generated by satellite-mounted magnetorquers. This actuation is an attractive solution for the long-term formation maintenance of multiple satellites, and has mainly been demonstrated for the two-satellite position control in a ground testbed. However, when the number of satellites  $N$  increases to more than three, this system contains fundamental challenges: 1) underactuation, 2) nonholonomic constraints, 3) scalability issues, and 4) high computational burden. To overcome these constraints, one practical solution is time-integrated current control, where the actuator outputs are time-varying, ensuring that the average acceleration matches the commanded value. We numerically and experimentally investigate two key aspects via time-varying magnetic actuation: (1) enhanced controllability on averaged dynamics with the theoretically guaranteed error bound, and (2) decentralized current management. Our primary application is the distributed space antennas through the integration of autonomous robotics technology and phased-array antenna systems. To emulate the orbital dynamics as equivalently as possible, we designed a ground-based experimental setup using an air-bearing platform, where position control experiments were conducted with custom-designed coils. This study can work as a proof of concept along with the tutorial paper on electromagnetic spacecraft control.

**Index Terms**—distributed space system, satellite swarm antenna array, small satellite, electromagnetic formation flight, multi-agent system, nonholonomic system



(a) Distributed space antenna studied in [1, 2, 3].



(b) Ten two-axis magnetorquers mounted on a linear air track.

Fig. 1: Distributed space antenna concept and experiment testbed of time-integrated magnetic interaction control using electromagnetic force and torque simultaneously.

## I. INTRODUCTION

This study aims to experimentally validate the principle of large-scale satellite swarm control using magnetic field

interactions. Large-scale space structures have plenty of advantages for the scientific and commercial community. In particular, large space antennas enable high data rates with small ground terminals and offer resilient cellular-band communication. Since launch vehicle size constraints pose significant challenges for larger antennas, distributed space antennas in Fig. 6d are studied in [1, 2, 3] where multiple satellites form a virtual space antenna. This payload distribution enhances redundancy and mission flexibility while reducing thermal structure requirements.

The magnetic interaction generated by satellite-mounted magnetorquers (MTQs) is an attractive solution for the long-term formation maintenance of satellite swarms. This actuator has been widely used on Earth-orbiting satellites for attitude control. Electromagnetic Formation Flight (EMFF) extends this concept to relative position control, and technical demonstrations have been conducted on the ground and in microgravity [4, 5, 6, 7, 8, 9]. Previous studies [2] show the feasibility of distributed space antenna using MTQs under unstable orbital dynamics in low Earth orbit.

However, when the number of satellites  $N$  increases to more than three, the magnetic field system contains fundamental challenges: 1) underactuation, 2) nonholonomic constraints, 3) scalability issues, and 4) high computational burden. Previous technical demonstrations have primarily been shown in two-satellite systems, focusing on relative distance control, thereby overcoming the fundamental limitations and enabling more flexible control. The first constraint arises from a fundamental lack of control over degrees of freedom. Even if each satellite has a three-axis magnetic coil and applies direct current (DC) [4, 10, 11, 12, 13, 14, 15, 16], the total number of control inputs is limited to  $3N$ . This is insufficient to control the full  $6N$  degrees of freedom instantaneously. Previous studies have introduced additional attitude control resources such as a three-axis reaction wheel (RWs) and minimizing the unintended electromagnetic torque [14, 17, 18]. For large-scale satellite systems, however, reducing the mass of these additional systems allows for greater resource allocation to other mission components, thereby improving mission efficiency. The second challenge is the nonholonomic constraint due to angular momentum conservation. MTQ control can not control all absolute positions and attitudes of multi-agents from the viewpoint of a holonomic and nonholonomic system, i.e., the entire linear and angular momentum remains unchanged. This is another reason most previous studies of EMFF assume that all satellites have RWs; all states in this system cannot be converged into the desired state by smooth state feedback [19]. The magnetic outputs must strictly satisfy this at every moment, and it must be explicitly accounted for in control design. EMFF requires complicated control scheme specific to the system because nonholonomic mechanical systems become uncontrollable by linearization; it is worth noting that the angular momentum exchange is available with the geomagnetic field in low Earth orbit, which relaxes this constraint. For these two problems, linearization leads to uncontrollability. Then, traditional linear

control theory is not applicable without a proper strategy. The third challenge concerns scalability, as each satellite is affected by the magnetic fields of all other satellites. Even though electromagnetic forces decay with the fourth power of distance, satellites experience undesired magnetic disturbances from non-cooperative neighbors.

To overcome these constraints, one of the practical solutions is a time-integrated current control: the actuator outputs are time-varying such that the average acceleration matches the commanded value. A previous study proposes a time-scheduled switching topology [10]: only two certain satellites generate DC magnetic interaction during a specific interval. A dipole polarity switching method [11] periodically changes dipole signs primarily for removing the Earth's magnetic field interaction. This technique can be extended to a solution to our problem in principle. Trajectory-level control, where satellites dynamically adjust their positions or orientations to generate virtual nonholonomic effects [20]. Another systematic approach is sinusoidal modulation of current and alternating current (AC) methods [5, 6, 7, 8, 9, 17, 21, 22, 23], adjusting both the phase [6, 17, 21] and frequency [7, 8, 9, 17, 23]. This naturally separates the strong coupling of the multiple satellite's and earth's magnetic interaction on averaged dynamics [7, 8, 17, 23] and offers control over many variables can be used to optimize the electromagnetic torque. A previous study investigated the time-averaging approach combined with this approach [24].

We numerically and experimentally investigate two key aspects via time-varying magnetic actuation: (1) enhanced controllability with the theoretically guaranteed error bound, and (2) decentralized current management. We use alternating current (AC) methods to generate time-averaged forces and torques. In this approach, the  $N$  satellite system is partitioned into multiple  $M \ll N$  satellite groups, and inter-group interactions are approximately decoupled on average. While our experiments focus on the case of  $M = 2$ , its extension to  $M \geq 3$  is possible through integration with the previous framework [25], leading to improved power-optimal control. Note that we only focus on the actuator-level time-varying control; Since small-time local controllability [26] is satisfied by EMFF [20], this guarantees asymptotically steer arbitrary states to any desired state due to the existence of continuous periodic feedback laws [27] and piecewise analytic feedback laws [28]. In this study, however, we omit this trajectory-level time-varying control since the accessibility of the Earth's magnetic field enables the actuator-level time-varying control (please refer to [20] for the trajectory-level study in EMFF). We demonstrate the feasibility of cooperative control in magnetically actuated satellite swarms through numerical simulations and experimental validation.

## II. PRELIMINARY, PROBLEMS AND OUR SOLUTION

This section introduces the magnetic field interaction based satellite control. Our mathematical notation about vector and coordination are follow: Let  $\{\mathbf{a}\}$  be defined as basis vector of an arbitrary frame ( $A$ ) such that  $\{\mathbf{a}\} = \{\mathbf{a}_x^T, \mathbf{a}_y^T, \mathbf{a}_z^T\}^T$

and we define  ${}^a p$  component of an arbitrary vector  $\mathbf{p} \in \mathbb{R}^3$  in this frame, i.e.,  $\mathbf{p} = \{\mathbf{a}\}^\top {}^a p = \{\mathbf{b}\}^\top {}^B p = \{\mathbf{b}\}^\top C^{B/A} {}^A p$  where  $C^{B/A} \in \mathbb{R}^{3 \times 3}$  is the coordinate transformation matrix from frame (A) to (B).

### A. Electromagnetic Force and Torque Model and Kinematics Command Modification for Nonholonomy

This subsection introduces the exact magnetic interaction model (near-field model) and its approximation (far-field model).

**Assumption 1.** We model the 1-axis coil as a circular air-core coil and define its dipole moment as  $\mu_a \triangleq \mu_{a0} \mathbf{n}$  and  $\mu_{a0} \triangleq N_t A c_a$  where the number of coil turns  $N_t$ , the area enclosed by the coil  $A$ , the current strength  $c_a(t)$ , and  $\mathbf{n}$  is the unit vector perpendicular to the plane of the coil.

Then, the exact magnetic field model  $B(r)$  [T] [14, 29] using the well-known Biot-Savart law is

$$B(r) = \frac{\mu_0 c}{4\pi} \oint \frac{dl \times \hat{r}}{|r|^2} \in \mathbb{R}^3.$$

where the magnetic permeability  $\mu_0$ , the coil element  $dl \in \mathbb{R}^3$ , and the distance between coil elements  $r \in \mathbb{R}^3$ . Then, the electromagnetic force and torque experienced by the  $b$ th 1-axis coil due to the magnetic field generated by the  $a$ th 1-axis coil is

$$\begin{aligned} f_{b \leftarrow a}^{\text{coil}} &= \frac{\mu_0 \mu_{a0} \mu_{b0}}{4\pi A^2} \oint \left[ \oint \frac{\mathbf{e}_{r_{ab}} \times dl_a}{r_{ab}^2} \right] \times dl_b \\ \tau_{b \leftarrow a}^{\text{coil}} &= \frac{\mu_0 \mu_{a0} \mu_{b0}}{4\pi A^2} \oint R_b \times \left[ \oint \frac{\mathbf{e}_{r_{ab}} \times dl_a}{r_{ab}^2} \right] \times dl_b. \end{aligned}$$

where  $\mathbf{e}_{r_{ab}}$  is unit vector along with  $r_{ab}$ ,

$$r_{ij} = s_{ij} + C^{i/j} R_j - R_i, \quad R_{i(\varphi)} = [R_i \cos \varphi, R_i \sin \varphi, 0]^\top$$

and  $dl_{i(\varphi)} = (dR_{i(\varphi)})/d\varphi d\varphi$ . Figure 2a provides an overview of each of these parameters. We assume the satellite specification to extend the above concept:

**Assumption 2.** All  $n$  satellites have the identical circular triaxial air-core coils, such that this defines the  $j$ th dipole moment of the multi-layer coil  $\mu_j(t) \in \mathbb{R}^3$  [Am<sup>2</sup>] at time  $t$ :

$$\mu_j(t) = \{\mathbf{b}\}^\top N_t A \begin{bmatrix} c_{jx}(t) \\ c_{jy}(t) \\ c_{jz}(t) \end{bmatrix} \triangleq \{\mathbf{b}\}^\top \begin{bmatrix} \mu_{jx}(t) \\ \mu_{jy}(t) \\ \mu_{jz}(t) \end{bmatrix} \quad (1)$$

where the current strength  $c_{j(x,y,z)}(t)$  along with  $x, y, z$ -axis in  $j$ th body-fixed frame.

Then, the electromagnetic force and torque on the  $j$ -th satellites due to the neighbor satellites  $\mathcal{N}_j$  is

$$\begin{bmatrix} \mathbf{f}_j \\ \boldsymbol{\tau}_j \end{bmatrix} = \sum_{k \in \mathcal{N}_j} \begin{bmatrix} \mathbf{f}_{j \leftarrow k} \\ \boldsymbol{\tau}_{j \leftarrow k} \end{bmatrix} = \sum_{k \in \mathcal{N}_j} \sum_{\substack{a= \\ (x,y,z)}} \sum_{\substack{b= \\ (x,y,z)}} \begin{bmatrix} \mathbf{f}_{j(a) \leftarrow k(b)}^{\text{coil}} \\ \boldsymbol{\tau}_{j(a) \leftarrow k(b)}^{\text{coil}} \end{bmatrix} \quad (2)$$

This model includes a circulant integration term that incorporates the relative position, relative attitude, and coil geometry, and a notable drawback is the heavy computational load.

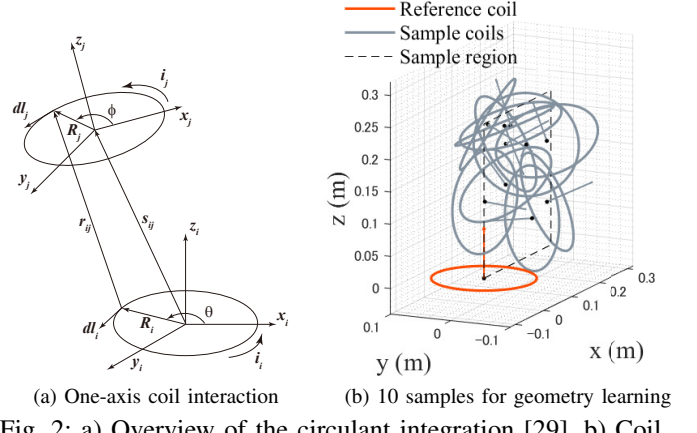


Fig. 2: a) Overview of the circulant integration [29], b) Coil geometry learning presented in subsection III-C

Then, a “Far-field” model [14] provides a computationally friendly approximated magnetic field. We define the relative vector  $s_{ij} \in \mathbb{R}^3$  between the geometric center of two coils, and the position vector  $R_i \in \mathbb{R}^3$  from the geometric center into  $dl_i$  such that  $r_{ij} = s_{ij} - R_i$ . We assume the size of the coil loop is much smaller than the relative distance, i.e.,  $|R_i| \ll |s_{ij}|$ . Then, we get

$$|R_i| \ll |s_{ij}| \Rightarrow \frac{1}{|r|} \approx \frac{1}{|s_{ij}|} + \frac{s_{ij} \cdot R_i}{|s_{ij}|^3}$$

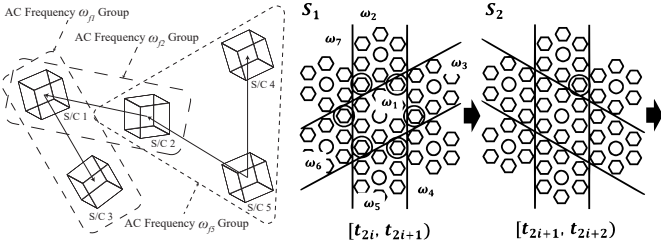
This approximation convert the multi-layer coil derives dipole model, i.e.,  $j$ th magnetic moment  $\mu_j(t) \in \mathbb{R}^3$  [Am<sup>2</sup>] at time  $t$  and its magnetic field  $B_k(\mu_k, r_{jk}) \in \mathbb{R}^3$  [T] are

$$B_k(\mu_k, r_{jk}) = \frac{\mu_0}{4\pi d_{jk}^3} (3M_k \mathbf{e}_r - \mu_k)$$

where  $\mu_k$  is in Eq. (1),  $M_k = \mu_k \cdot \mathbf{e}_r$ ,  $d_{jk} = \|r_{jk}\|$ , and  $\mathbf{e}_r = r_{jk}/d_{jk}$ . This model is accurate if the relative distance  $s_{ij}$  exceeds around twice the diameter of the coil, i.e.,  $2R_i$  [13]. This also simplifies the magnetic field interaction model, the electromagnetic force and torque exerted on the  $j$ -th agent by the  $k$ -th one as  $\mathbf{f}_{j \leftarrow k}(\mu_{j,k}, r_{jk}) = \nabla(\mu_j \cdot B_k)$  and  $\boldsymbol{\tau}_{j \leftarrow k}(\mu_{j,k}, r_{jk}) = \mu_j \times B_k$  where

$$\mathbf{f}_{j \leftarrow k} = \frac{3\mu_0}{4\pi d^4} ((\mu_k \cdot \mu_j - 5M_k M_j) \mathbf{e}_r + M_k \mu_j + M_j \mu_k). \quad (3)$$

We derive the command value of electromagnetic force and torque that satisfies angular momentum conservation using “EMFF Kinematics” [20, 24, 30]. We consider the  $n$  satellites with 3-axis MTQ and assume that  $m \in [1, n]$  satellites are equipped with 3-axis RWs. We define the tangent space of angular momentum conservation  $S_{(n,m)} \in \mathbb{R}^{(6n+3m) \times (6n+3m-3)}$ , i.e.,  $S_{(n,m)} \in \text{Null Space}(A_{(n,m)})$



(a) Multi-leader guidance [25] (b) Token-based maneuvering [10, 24]

Fig. 3: Examples of decoupled maneuvering (a) Multi-leader guidance protocol: Five satellites are divided into three groups with three AC frequencies:  $\omega_{f1}$ ,  $\omega_{f2}$ , and  $\omega_{f3}$ , (b) token-based decoupled maneuvering with AC modulation: satellites operate in a sequence  $S = \{S_1, S_2, \dots, S_N\}$  where  $S_i$  is the set of active vehicles during time interval  $[t_i, t_{i+1}]$ .

where  $A_{(n,m)} \in \mathbb{R}^{3 \times (6n+3m)}$

$$\sum_{j=1}^n \left( m_j \mathbf{r}_j \times \frac{d\mathbf{r}_j}{dt} + \mathbf{I}_j \cdot \boldsymbol{\omega}_j \right) + \sum_{j=1}^m \mathbf{h}_j = \mathbf{L} \Leftrightarrow \\ A_{(n,m)} \begin{bmatrix} \dot{\mathbf{r}}^i \\ \mathbf{w}^b \\ \xi^b \end{bmatrix} = \begin{bmatrix} m_1[\dot{\mathbf{r}}^i]_1, \dots, m_n[\dot{\mathbf{r}}^i]_n, \\ C^{I/B_1} J_1, \dots, C^{I/B_n} J_n, \\ C^{I/B_1}, \dots, C^{I/B_m} \end{bmatrix} \begin{bmatrix} \dot{\mathbf{r}}^i \\ \mathbf{w}^b \\ \xi^b \end{bmatrix} = 0$$

where  $\xi^b \in \mathbb{R}^{3m}$ , and  $\xi_j^{bj} = h_j^{bj} - \frac{1}{m} L^{bj}$ . The command values based on these fields could be generated by MTQ. Using these formulation, we can construct the nonlinear non-convex optimization problem  $\mathcal{OPT}_{DC}$  to allocate to achieve simultaneous control:

#### $\mathcal{OPT}_{DC}$ : DC-based Optimal Dipole Allocation Problem

$$\begin{cases} \min. J(\mu_{1(x,y,z)}, \dots, \mu_{n(x,y,z)}, \chi) \\ \text{s.t. } \{f_{cj}, \tau_{cj}\} = \sum_{k \neq j} \{f_{j \leftarrow k}, \tau_{j \leftarrow k}\} \text{ for } j = 1, \dots, N \end{cases}$$

where  $J \in \mathbb{R}$  is arbitrary evaluation function with arbitrary parameters  $\chi$ .

#### B. Time-Integrated Control for Underactuated Allocation, Scalability, and Computation

This subsection introduces the time-integration current control to overcome the underactuation. We first demonstrate the necessity of time-integrated current control to extend controllability, i.e., simultaneously control both electromagnetic force and torque. This is highlighted by the polynomial formulations of the magnetic interaction [14, 24, 30], which is helpful to check the availability of simultaneous control. The far-field approximation in Eq. (3) and  $\mathcal{OPT}_{DC}$  can be simplified to a multivariate bilinear system of polynomial equations and results equivalent problem  $\mathcal{OPT}_{DC}^{Bilinear}$ :

#### $\mathcal{OPT}_{DC}^{Bilinear}$ : DC-based Optimal Dipole Allocation Problem

$$\begin{cases} \min. J(\mu_{1(x,y,z)}, \dots, \mu_{n(x,y,z)}, \chi) \\ \text{s.t. } \underbrace{f_{cj(x,y,z)}, \tau_{cj(x,y,z)}}_{= \text{Const. command input}} = \sum_{k=1}^3 \sum_{l=1}^n \sum_{m=1}^3 \underbrace{\mu_{jk}}_{\text{Variable}} \underbrace{C_{jklm}}_{\text{Const.}} \underbrace{\mu_{lm}}_{\text{Variable}} \end{cases}$$

where  $C_{jklm} \in \mathbb{R}$  is the constant value associated with the state of the system. Since this problem includes  $3n$  variables and  $6n-6$  polynomials, DC-based magnetic field control can generate arbitrary electromagnetic forces or torques for  $n$  satellites or achieve simultaneous control only for two satellites. This is the one reason that most previous studies (which even included AC-based EMFF) used only electromagnetic force, considering torque as a disturbance.

#### 1) Time-Integrated Control of Alternating Current

We next consider the AC method to explain how the time-integrated current control expands the controllability by AC modulation technique. We assume that  $j$ th satellite's MTQ for  $j \in [1, n]$  are driven sinusoidal with angular frequency  $\omega_j [\text{rad/s}]$ . Here, we assume that  $a, b$ th dipole and the time-varying electromagnetic force and torque are written down

$$\begin{cases} \boldsymbol{\mu}_a(t) = \boldsymbol{\mu}_a^{\text{amp}} \sin(\omega_a t + \theta), \quad \boldsymbol{\mu}_b(t) = \boldsymbol{\mu}_b^{\text{amp}} \sin(\omega_b t) \\ f_{b \leftarrow a}, \tau_{b \leftarrow a}(t) = (\kappa_1(t) + \kappa_2(t)) \mathbf{f}, \boldsymbol{\tau}(\boldsymbol{\mu}_a^{\text{amp}}, \boldsymbol{\mu}_b^{\text{amp}}, \mathbf{r}_{ba}) \\ \kappa_1(t), \kappa_2(t) = \pm \frac{1}{2} \cos((\omega_a \mp \omega_b)t + \theta) \end{cases}$$

where amplitudes  $\mu_{\text{amp}} \in \mathbb{R}^3$  and the phase differences  $\theta \in \mathbb{R}^3$  that are constant during specific one cycle  $T$ . This shows  $\mathbf{f}, \boldsymbol{\tau}$  take 0 in first-order averaged dynamics and the different angular frequencies' agents do not interact with each other.

$$\begin{cases} \mu_j(t) = \mu_j^{\text{DC}}(t) + \sum_{k \in \mathcal{N}_j} \mu_j^{\sin} \sin \omega_j t + \mu_j^{\cos} \cos \omega_j t \\ f_{j \leftarrow k}^{\text{avg}} \triangleq \frac{1}{2} \sum_{k \neq j} \{f(\mu_k^{\sin}, \mu_j^{\sin}, r_{jk}) + f(\mu_k^{\cos}, \mu_j^{\cos}, r_{jk})\}. \end{cases}$$

After these notations, the AC-based current control derives  $f_j^{\text{avg}}$  and  $\tau_j^{\text{avg}}$  are  $\psi = f_{j \leftarrow k}^{\text{avg}}$ . We can also simplify

#### $\mathcal{OPT}_{AC}^{\text{Bilinear}}$ : AC-based Optimal Dipole Allocation Problem

$$\begin{cases} \min. J(\mu_{1(x,y,z)}^{\sin}, \dots, \mu_{n(x,y,z)}^{\sin}, \mu_{1(x,y,z)}^{\cos}, \dots, \mu_{n(x,y,z)}^{\cos}, \chi) \\ \text{s.t. } \underbrace{f_{cj(x,y,z)}, \tau_{cj(x,y,z)}}_{= \text{Const. command input}} = \sum_{k \neq j} \{f_{j \leftarrow k}^{\text{avg}}, \tau_{j \leftarrow k(x,y,z)}^{\text{avg}}\} \\ = \sum_{k=1}^3 \sum_{l=1}^n \sum_{m=1}^3 \left( \underbrace{\mu_{jk}^{\sin}}_{\text{var.}} \underbrace{C_{jklm}^{\sin}}_{\text{const.}} \underbrace{\mu_{lm}^{\sin}}_{\text{var.}} + \underbrace{\mu_{jk}^{\cos}}_{\text{var.}} \underbrace{C_{jklm}^{\cos}}_{\text{const.}} \underbrace{\mu_{lm}^{\cos}}_{\text{var.}} \right) \end{cases}$$

where  $j = 1, \dots, N$ ,  $C_{jklm}^{\sin} \in \mathbb{R}$  and  $C_{jklm}^{\cos} \in \mathbb{R}$  are also the constants associated with the state of the system for sin and cos. This problem includes  $6n$  variables and  $6n-6$  polynomials. A system of  $k$  polynomial equations in  $k$  variables generally gave  $d = \prod_{l=1}^k d_l$  isolated solutions, where  $d_l$  denotes the highest degree of the  $l$ th equation and  $d_l = 2$  for our case. Then, equality constraints in  $\mathcal{OPT}_{AC}^{\text{Bilinear}}$  potentially have  $2^{6n-6}$  solutions and 6 free dipole moments. Since there are more variables than equations, simultaneous control may well be realized even for  $n$  satellites. Note that these solutions can include not physically implementable solution, i.e., “solutions at infinity” [31].

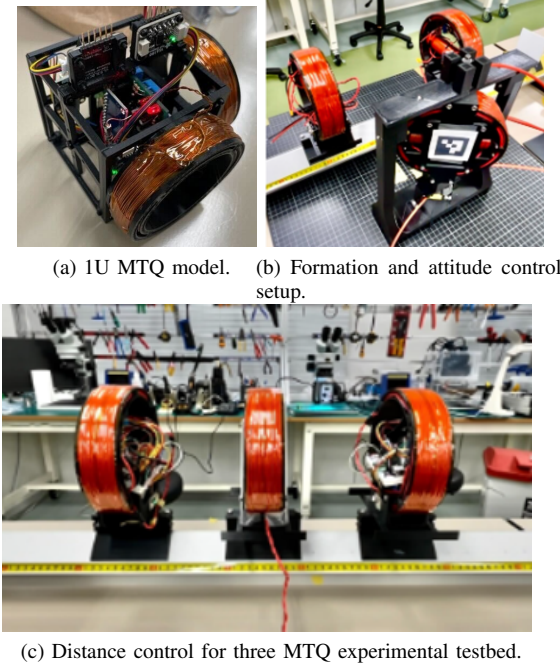


Fig. 4: Two type custom-built two-axis magnetorquers and experimental overview for formation and attitude control.

## 2) Practical Time-interated Maneuvering

It is worth noting that the principle of this subsection may well be extended to an arbitrary time-integrated control framework, which is especially suitable for practical implementation. This extension is future work.

## III. EXPERIMENTAL REQUIREMENT

We provide a brief overview of the experimental setup. As illustrated in Figs. 6f, 4b, and 4c, the testbed consists of a 1.5 m linear air track (Eisco, PH0362A) with an associated air blower (Eisco, PH0363A), and a single-axis air bearing. The white reflectors for distance sensing are placed on MTQs and both ends of the linear track in the appropriate orientation. The custom-built magnetorquers (MTQs) are mounted on 100g gliders that move along the linear track, while some MTQ is installed on the air bearing, allowing for frictionless rotation about a single axis. The mechanical constraints of the linear track are accounted by ensuring that the net force acts along the track's direction. This setup enable a partial validation of the experimental feasibility of 6-DoF control using a combination of the air bearing and linear air track. For given the constant target position  $p_d \in \mathbb{R}^N$ , such as truss formation, and target velocity  $v_d = \dot{p}_d = 0$ , we define the error states between the perturbed system and the unperturbed target states, i.e.,  $p_e = p - p_d$  and  $v_e = v - v_d$ . Then, a given fixed graph  $\mathcal{G}$  define edge states of the agents on ground experiment,  $e_{p_e} = E^\top p_e$ ,  $e_{v_e} = E^\top v_e$ , and  $\dot{e}_{v_e} = E^\top (u + d)$ . Its state equation is

$$\frac{d}{dt} \begin{bmatrix} e_{v_e} \\ e_{p_e} \end{bmatrix} \triangleq \underbrace{\begin{bmatrix} -E^\top K_d & -E^\top K_p \\ I & O \end{bmatrix}}_{A_{\text{gnd}}} \begin{bmatrix} e_{v_e} \\ e_{p_e} \end{bmatrix} + \begin{bmatrix} E^\top d \\ 0 \end{bmatrix} \quad (4)$$

### A. Time Constant Requirement for Orbital Operation

This subsection describes the time constant requirement of the ground experiment that is consistent with on-orbital operation. Along with the state estimation period  $T_e$ , two key time scales for our system arise: the control input update period  $T_c$ , and the averaging duration  $T_{\text{avg}}$ . We distinguish two major regimes for time-scale design: the initial transient phase and the steady-state phase. Attitude control of a monolithic satellite or satellite formation control using thrusters can often be modeled as a single-input single-output (SISO) system. In contrast, formation control based on magnetic interactions inherently relies on inter-satellite coupling, causing the overall system time constant to depend on the number of satellites  $N$ .

#### 1) Relative Orbital Dynamics in Earth Orbit

We first introduce the relative orbital dynamics of the orbiting satellites. This subsection mainly uses an orbitally fixed coordinate system  $\mathcal{O}$  system whose basis is

$$\mathbf{o}_x = \text{nor}(\mathbf{r}), \quad \mathbf{o}_y = \mathbf{o}_z \times \mathbf{o}_x, \quad \mathbf{o}_z = (\mathbf{r} \times \dot{\mathbf{r}})/\|\mathbf{r} \times \dot{\mathbf{r}}\|$$

where  $\mathbf{r} \in \mathbb{R}^3$  is the position vector from the Earth's center. We define the relative position of the  $j$ -th satellite from the  $k$ th satellite as  $r_{jk} = r_j - r_k = [x_{jk}; y_{jk}; z_{jk}]$ . Then, linearization around the reference orbit yields the relative motion dynamics in  $\{\mathcal{O}\}$  [32, 33]:

$$\begin{aligned} \ddot{\bar{x}} - 2\omega_{xy}\dot{\bar{y}} - 3\omega_{xy}^2\bar{x} - \frac{4\omega_{xy}^2}{c_-^2/s_{J_2}} \left( 2\bar{x} + \frac{\dot{\bar{y}}}{\omega_{xy}} \right) &= c_+ u_x \\ \ddot{\bar{y}} + 2\omega_{xy}\dot{\bar{x}} &= c_- u_y, \quad \ddot{\bar{z}} + \omega_z^2\bar{z} = h(\cdot) + u_z \end{aligned}$$

where  $u_{x,y,z} \in \mathbb{R}$  are input including disturbance,  $\bar{x} = c_+ x$ ,  $\bar{y} = c_- y$ ,  $c_\pm = \sqrt{1 \pm s_{J_2}}$ ,  $s_{J_2}(i_{\text{ref}}) \approx 1e^{-4}$ ,  $h(\cdot) = 2l_z\omega_z \cos(\omega_z t + \theta_z)$ ,  $\epsilon_2 \approx (3 + 5e^{-4})\omega_{xy}$ ,  $\omega_{xy} = c_- \sqrt{\mu/r_{\text{ref}}^3}$  and  $\omega_z$  and  $l_z$  are. Here, integrating this equation derives the analytical solution:

$$\begin{bmatrix} x_{jk}(t) \\ y_{jk}(t) \\ z_{jk}(t) \end{bmatrix} = \begin{bmatrix} 2C_{1(0)} + r_{xy} \sin(\omega_{xy}t + \theta_{xy})/c_+ \\ C_{4(0)} - \epsilon_2 C_{1(0)}t + 2r_{xy} \cos(\omega_{xy}t + \theta_{xy})/c_- \\ (r_z + l_z t) \sin(\omega_z t + \theta_z) \end{bmatrix}$$

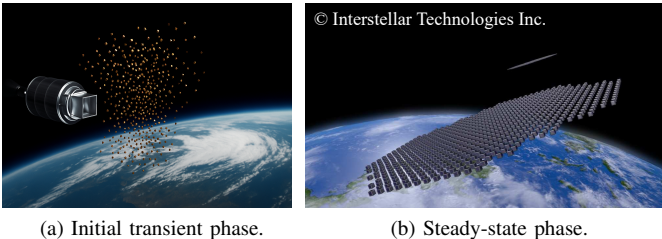
where averaged  $J_2$  relative orbital parameters: drift motion coefficient  $C_1$  and relative orbit centre coefficient  $C_4$

$$C_1 = \frac{c_+}{c_-^2} \left( 2\bar{x} + \frac{\dot{\bar{y}}}{\omega_{xy}} \right), \quad C_4 = \frac{1}{c_-} \left( \bar{y} - \frac{2\dot{\bar{x}}}{\omega_{xy}} \right).$$

This analytical solution shows that the relative orbital motion includes the drift and periodic terms. These drift terms cause the control loss of MTQ based on its distance-based nature. Then, we apply the  $u_y = -$  for the low input constraint and its closed-loop system is

$$\begin{bmatrix} \dot{e}_1 \\ \dot{e}_4 \end{bmatrix} = \underbrace{\begin{bmatrix} -\frac{k_A}{2}L_e & O \\ \frac{\epsilon_2}{2} \left( I - \frac{k_1\gamma}{2}L_e \right) & -\frac{\gamma k_A}{2}L_e \end{bmatrix}}_{A_{\text{orb}}} \begin{bmatrix} e_1 \\ e_4 \end{bmatrix} - k_0 \begin{bmatrix} E^\top D_y \\ E^\top D_x \end{bmatrix} \quad (5)$$

where  $e_1 = E^\top [-2C_1]$ ,  $e_4 = E^\top [C_4]$  using the associated the incidence matrix that caputure the satellites coordination,



(a) Initial transient phase. (b) Steady-state phase.

Fig. 5: Two major regimes and guidelines for time-scale design: a)  $T_c = (k\lambda_{\max}n_{\text{safe}})^{-1}$ , b)  $T_c = \min\left\{\frac{1}{2n_{\text{safe}}f_d}, \frac{1}{k\lambda_{\max}n_{\text{safe}}}\right\}$ ,  $T_{\text{avg}}(k\lambda_2)^{-1}$

$k_0$  is averaged  $J_2$  dynamics constant as  $k_0 = 2c_+ / (\omega_{xy}c_-)$ . Therefore, we mainly consider this agreement protocol, i.e.,  $\dot{x} = -kLx$ , and the analytical solution is

$$x(t) = \underbrace{e^{(-kLt)}x(0)}_{\text{Initial transient term}} + \underbrace{\int_0^t e^{(-kL(t-\tau))}d(\tau) d\tau}_{\text{Steady-state error term}} \quad (6)$$

where  $e^{(-kLt)}x(0) = \sum_{i=1}^N (v_i^\top x(0)) e^{-k\lambda_i t} v_i$  and  $v_i \in \mathbb{R}^N$  is the eigenvector corresponding the eigenvalues  $\lambda_i \in \mathbb{R}$  that holds  $0 = \lambda_1 < \lambda_2 \leq \dots \leq \lambda_N$  under the connected conditions. During the transient phase, high-frequency components associated with  $\lambda_N$  dominate. From a signal processing perspective, aliasing occurs when the sampling frequency is too low to capture these high-frequency modes, causing distortion. To ensure stability and prevent aliasing, the control update period must satisfy  $T_c \leq 1/(k\lambda_{\max}n_{\text{safe}})$ , where  $k$  is the feedback gain and  $n_{\text{safe}} \in \mathbb{N}_+$  is a safety margin. To limit  $\lambda_{\max}$ , we made the following assumption:

**Assumption 3.** Each satellite interacts with at most  $\Delta$  others.

This can be realized by centralized grouping, such as [3], and derives  $\lambda_{\max} \leq 2\Delta$ , e.g.,  $\Delta = 6$ . After transients decay, low-frequency modes and disturbances prevail. If the disturbance has a known fundamental frequency  $f_d$ , the Nyquist criterion gives  $T_c \leq \frac{1}{2f_d}$ . If the spectrum is broadband or unknown, a conservative bound is

$$T_c \leq \min\left(\frac{1}{2f_d}, \frac{1}{k\lambda_{\max}N}\right) \leq \min\left(\frac{1}{2f_d}, \frac{1}{k\Delta N}\right).$$

For time-scale separation, the system evolves on a finer scale  $y(t, \tau)$ , and the averaged dynamics are defined as

$$\frac{dx}{dt} = -kLx = \int_0^T \frac{dy}{d\tau}(t, \tau) \frac{d\tau}{T} \Rightarrow T \ll \frac{1}{k\lambda_2} \quad (7)$$

To validate this approximation, the averaging window must be much smaller than the slowest mode's time scale. To partially ensures dynamical equivalence between the ground testbed and the on-orbit system, we assume that there exist the coordinate transformation  $\Theta \in \mathbb{R}^{2n \times 2n}$ :

$$\begin{aligned} \begin{bmatrix} \mathbf{e}_1 \\ \mathbf{e}_4 \end{bmatrix} &\triangleq \Theta \begin{bmatrix} \mathbf{e}_{v_e} \\ \mathbf{e}_{p_e} \end{bmatrix} = \begin{bmatrix} \Theta_{11} & \Theta_{12} \\ O & \Theta_{22} \end{bmatrix} \begin{bmatrix} \mathbf{e}_{v_e} \\ \mathbf{e}_{p_e} \end{bmatrix} \\ \text{s.t. } \frac{\Theta A_{\text{gnd}}}{\beta} &= A_{\text{orb}}\Theta, \quad \beta \approx \frac{\|\Theta_{11}E^\top d\|_\infty}{\|k_0 E^\top D_y\|_\infty}, \quad \tau \triangleq \beta t \end{aligned} \quad (8)$$

where  $A_{\text{gnd}}$  is Eq. (4) and  $A_{\text{orb}}$  is Eq. (5) where  $\beta$  is the disturbance ratio.

**Theorem III.1.** There exists a coordinate transformation matrix such that

$$\Theta_{11} = P(L_e) = \sum_{m=0}^r \alpha_m L_e^m, \quad \alpha_0 \neq 0 \quad (9)$$

and  $\Theta_{12}$  and  $\Theta_{22}$  in Eq. (11) for the closed-loop system applied a second-order Laplacian gain controller

$$u = -\frac{\beta k_A}{2} \left( k_v - \frac{\beta k_A}{2} \right) L^2(p - p_d) - k_v L(v - v_d) \quad (10)$$

*Proof:* We temporarily define  $u = -K_p(p - p_d) - K_d(v - v_d)$ . The relationship  $\Theta A_{\text{gnd}} = \beta A_{\text{orb}}\Theta$  in Eq. (10) is equivalent to the four block relations

- (i)  $-\Theta_{11}E^\top K_d + \Theta_{12} = \beta A_{11}\Theta_{11}$
- (ii)  $-\Theta_{11}E^\top K_p = \beta A_{11}\Theta_{12}$ ,
- (iii)  $\Theta_{22} = \beta A_{21}\Theta_{11}$ ,
- (iv)  $0 = \beta(A_{21}\Theta_{12} + A_{22}\Theta_{22})$ .

Since  $\Theta_{11}$  need to be commute with  $L_e$ , we choose it as invertible polynomial function  $P(L_e)$  in Eq. (9) and this derives  $\Theta_{12}$  and  $\Theta_{22}$  as

$$\Theta_{12} = \Theta_{11}(E^\top K_d - \beta A_{11}), \quad \Theta_{22} = \beta A_{21}\Theta_{11} \quad (11)$$

where  $A_{11} = -\frac{k_A}{2}L_e$  and  $A_{22} = -\frac{\gamma k_A}{2}L_e$ . Substituting the above into (ii) and cancelling the commuting, nonsingular  $\Theta_{11}$  condition gives

$$\beta^2 A_{11}^2 + \beta A_{11} E^\top K_d + E^\top K_p = 0 \quad (12)$$

Here, constraining  $E^\top K_p \propto L_e$  i.e. degree 1, forces  $k_p = 0$  that results absence of proportional term. To avoid this, we choose  $E^\top K_d = k_v L_e$  and  $E^\top K_p = k_p L_e^2$  such that

$$\left( \frac{\beta^2 k_A^2}{4} - \frac{\beta k_A k_v}{2} + k_p \right) L_e^2 = 0 \Rightarrow k_p = \frac{\beta k_A}{2} \left( k_v - \frac{\beta k_A}{2} \right).$$

As a result, we confirm a second-order Laplacian gain  $K_p \propto L_e^2$  in Eq. (10). ■

Multiplying  $\Theta$  and  $\beta^{-1}$  from left of Eq. (4) yields

$$\frac{d}{d(\beta t)} \begin{bmatrix} \mathbf{e}_1 \\ \mathbf{e}_4 \end{bmatrix} = A_{\text{orb}} \begin{bmatrix} \mathbf{e}_1 \\ \mathbf{e}_4 \end{bmatrix} + \frac{1}{\beta} \begin{bmatrix} \Theta_{11} E^\top d \\ 0 \end{bmatrix}$$

Then, we select any invertible  $\Theta_{11} = P(L_e)$  and  $k_v > \beta k_A / 2$  and this derives  $k_p$  and  $\Theta_{12,22}$ , dependently. The time-scale transformation  $t_{\text{gnd}} = t_{\text{orb}} / \beta$  scales command updata period  $T_s$  and coordinate transformation  $\Theta$  map ground-frame errors to orbital-frame errors one-to-one.

## 2) Attitude Controller Design in Earth Orbit

The main disturbance torques for attitude motion are placed on two frequency bands: the orbital one  $\omega_o \sim 1.1\text{e}^{-3}$  rad/s, e.g., the residual magnetic and gravity tilt torque, and user-defined dipole frequencies  $\omega_f \in \omega_{fs} = [\underline{\omega}_f, \bar{\omega}_f]$ . In this study, the majority of attitude control is assumed to rely on interactions with the geomagnetic field, effectively decou-

pling satellites from each other. Note that this torque model is often used to realize a cross-product attitude controller  $\tau_{MTQ} = -[B_e] \times d_{DC}$  with geomagnetic field  $B_e$ . In practice, we may well account for the number of satellites for attitude control, and this is a future work.

### B. Experimental Hardware Design

We summarize the sequential MTQ parameter selection to decide the specification of designed coils in Fig 4. We consider the decision parameters of coil design are the following four Multilayer coil and others became dependent variable as a result of the design process:

- Inner and outer coil diameters  $\underline{D}, \bar{D}$  [m]. Multilayer coil diameter  $D_{coil} = (\underline{D} + \bar{D})/2$
- Circuit voltage  $V_{cir}$  [V]
- Upper current  $\bar{c}_{wire}$  [A]
- Coil height  $H_{coil}$  [m]

To evaluate the feasibility of the designed solution and approximation of the near-field model, we first conduct experiments where the long-range magnetic field model is valid. Subsequently, we assess the validity of the algorithm using the near-field model. Therefore, it is a prerequisite that experiments can be performed under the far-field approximation. The coil design requirement along with our values are the following four.

- 1) Disturbance force  $a_d$  [N/kg]: The micro-gravity due to the small distortion of the linear air track that is estimated  $\approx 0.01^\circ$  and thus  $|a_d| \approx 2(9.8 \sin(0.01^\circ)) \leq 4e^{-3}$ . Note that this  $a_d$  allows to move  $a_d t^2/2 \approx 0.2 - 0.8$  [m] within 10–20 seconds at a certain distance in a microgravity environment
- 2) Size constraint: Feasibility of dipole approximation on Eq. (3) for the coil diameter  $D_{coil}$  and operation distance  $r$ . the target distances and initial distances  $r_d, r_0$  [m] should be larger than  $2.5D_{coil}$ . The upper limit of the coil height was estimated to be A

Target & initial distances:  $r_d = 3D_{coil}$ ,  $r_0 = r_d + 0.1$

- 3) Maximum weight  $\bar{m}_{MTQ}$ : The linear air tracks can withstand  $\bar{m}_{MTQ} \approx 1.3$  from measurements.
- 4) Electric power balance: Discrete drive voltage  $\bar{V}_{cir}$  and corresponding mass of LiPo battery.

We find the appropriate wire to satisfies these requirements based on the following material information  $k_{\Omega/kg}$  [ $\Omega/kg$ ],  $k_{\Omega/m}$  [ $\Omega/m$ ],  $\bar{c}_{wire}$  [A],  $D_{wire}$  [m] We derive the dependent coil parameters for the design variables  $D_{coil}$  and circuit voltage  $\bar{V}_{cir}$  [V] by the following. At first, we calculate the 1-axis coil resistor.  $\Omega_{coil} = \min(\bar{V}_{cir}/\bar{c}_{wire}, \bar{m}_{coil} k_{\Omega/kg})$  such that the maximum current is lower than  $\bar{c}_{wire}$  and second is the mass constraint to satisfy  $m_{coil} \leq \bar{m}_{coil}$ . Next, we derives

- |   |
|---|
| $\left\{ \begin{array}{l} \text{The number of wiring [-]: } N_t = \Omega_{coil}/k_{\Omega/m}/(\pi D_{coil}) \\ \text{Maximum dipole [A/m}^2\text{]: } \bar{\mu} = \pi(D_{coil}/2)^2 N_t \bar{c}_{wire} \\ \text{Thickness of coil wire [m]: } t_{coil} = N_t/(H_{coil}/D_{wire}) \end{array} \right.$ |
|---|

Parameter	Optimization	Prototyping
satellite size $2a_{sat}$	11cm	10cm
coil diameter $2a_{coil}$	7.5cm	7.5cm
satellite mass $m_{sat}$	0.536kg	0.336kg
coil mass $m_{3coil}$	0.103kg	0.120kg

TABLE I: Distributed antenna design examples [2]

Finally, we calculate the optimization problem for maximizing the acceleration.

$$D_{coil}^*, \bar{V}_{cir}^* = \arg \min_{D_{coil}, V_{cir} \in \mathbb{R}} \frac{\bar{\mu}^2}{m_{coil}}$$

$$\text{s.t. } \begin{cases} m_{coil} = \frac{\Omega_{coil}(V, \bar{c}_{wire}, k_{\Omega/kg}, \bar{m}_{coil})}{k_{\Omega/kg}} \leq \bar{m}_{coil} \\ F(d_0) = \frac{1}{2} \frac{3\mu_0}{2\pi} \frac{\mu^2}{d^4} \geq a_d \\ t_{coil} \leq \frac{D_{coil}}{6} \end{cases}$$

We develop the MTQ for the iron/air core coil and for three materials: copper, polyester, and tin-plated copper. We applied a polyester-enamelled copper wire (PEW), and UL1070 with a thickness of about 0.5–2 mm was selected as a candidate for ease of design. This custom-made experience reveals the suitable application for each material and provides lessons learned for packing into the 1U-sized satellite.

**Remark 1.** Combining the previously developed comprehensive system design using non-convex optimization [2] confirms that the designed cubic MTQ in Fig. 4a satisfies long-term formation-keeping constraints to achieve a 1U-sized satellite swarm for low-Earth orbit (LEO) communication. Table ?? shows the derived optimal specifications of each axis coil. The power electronics comprise a lithium-polymer battery (800mAh, 35.6g) and a circuit (40g). However, micro-gravity on the linear air track is much larger than orbital ones, and this model could not cope with it. We evaluate the magnetic interaction system in an equivalent system in Eq. (8).

### C. Learning-based Coil-Specific Geometry Approximation

We design an approximate exact magnetic field model using a multilayer perceptron (MLP) model that captures coil-specific geometric features and calculates in real-time during the control experiment. The  $j$ -th electromagnetic force and torque due to the magnetic field generated by the  $k$ th satellite in Eq. (2)

$$\begin{bmatrix} {}^a f_{j \leftarrow k} \\ {}^a \tau_{j \leftarrow k} \end{bmatrix} = \frac{\mu_0}{4\pi A^2} \begin{bmatrix} {}^a I_{j \leftarrow k_x} & {}^a I_{j \leftarrow k_y} & {}^a I_{j \leftarrow k_z} \\ {}^a J_{j \leftarrow k_x} & {}^a J_{j \leftarrow k_y} & {}^a J_{j \leftarrow k_z} \end{bmatrix} ({}^a \mu_k \otimes {}^a \mu_j)$$

where  ${}^a I_{j \leftarrow k_x} = [{}^a I_{j_x \leftarrow k_x}, {}^a I_{j_y \leftarrow k_x}, {}^a I_{j_z \leftarrow k_x}] \in \mathbb{R}^{3 \times 3}$  and

$$\begin{cases} {}^a I_{j_x \leftarrow k_x} = \int_{\theta=0}^{\theta=2\pi} \left[ \int_{\varphi=0}^{\varphi=2\pi} \frac{{}^a \mathbf{e}_{r_{j \leftarrow k}} \times dl_{k_x}}{r_{j \leftarrow k}^2} \right] \times dl_{j_x} \\ {}^a J_{j_x \leftarrow k_x} = \int_{\theta=0}^{\theta=2\pi} R_{j_x} \times \left[ \int_{\varphi=0}^{\varphi=2\pi} \frac{{}^a \mathbf{e}_{r_{j \leftarrow k}} \times dl_{k_x}}{r_{j \leftarrow k}^2} \right] \times dl_{j_x}. \end{cases} \quad (13)$$

This circulant integration term includes the relative position, relative attitude, and coil geometry. Since an obvious drawback is a heavy computational load, we approximate these coil-specific geometry terms using a multi-layer perceptron (MLP). We first mention the sampling input and lable datas. For the  $k$ th satellite, we define  $\mathbf{n}_{k(x,y,z)}$  as the unit vectors along with  $x, y, z$  axes and derive coordinate frame  $B_{k(x,y,z)}$  such that each  $n_{k(x,y,z)}$  corresponds to its  $z$ -axis. Then the transformation matrixes  $C^{A/B_{k(x,y,z)}} \in \mathbb{R}^{3 \times 3}$  from the body-fixed frame  $B_{k(x,y,z)}$  to arbitrary frame A is given by

$$C^{A/B_{k(x,y,z)}} = [a n_{k(x,y,z)} \quad a n_{k(y,z,x)} \quad a n_{k(z,x,y)}] \quad (14)$$

To reduce the sampling number,  $\theta \triangleq \tan^{-1}(r(2), r(1))$

$$C^{D_{j \leftarrow k(x,y,z)}/B_{k(x,y,z)}} = \begin{bmatrix} \cos \theta & \sin \theta & 0 \\ -\sin \theta & \cos \theta & 0 \\ 0 & 0 & \text{sgn}(r(3)) \end{bmatrix} \quad (15)$$

As a result, our sampling data are stucted as follows:

$$\mathbf{x} = \begin{bmatrix} [d_r_{j \leftarrow k}^{(1)}; d_n_{jz}^{(1)}]^\top \\ \vdots \\ [d_r_{j \leftarrow k}^{(N_s)}; d_n_{jz}^{(N_s)}]^\top \end{bmatrix}, \quad \mathbf{y} = \begin{bmatrix} [d I_{j_z \leftarrow k_z}^{(1)}; d J_{j_z \leftarrow k_z}^{(1)}]^\top \\ \vdots \\ [d I_{j_z \leftarrow k_z}^{(N_s)}; d J_{j_z \leftarrow k_z}^{(N_s)}]^\top \end{bmatrix}$$

where  $N_s$  is the number of samples. Our MLP represents the functional mapping from given inputs  $\mathbf{x}$  into some outputs  $f(\mathbf{x}, \boldsymbol{\theta})$  such as a  $(L+1)$ -layer neural network and we train to minimize the squared-error loss function:

$$\theta_w^*, \theta_b^* = \underset{j=1}{\operatorname{argmin}} \sum_{j=1}^{N_s} \left( f \left( \left\| \mathbf{y}^{(j)\top} - \hat{\mathbf{y}}(\mathbf{x}^{(j)}, \boldsymbol{\theta})^\top \right\| \right) \right) \quad (16)$$

$$\hat{\mathbf{y}}(\mathbf{x}, \boldsymbol{\theta}) = W^{L+1} \phi(\cdots \phi(W^1 \mathbf{x} + b^1) \cdots) + b^{L+1}$$

where the activation function  $\phi(\cdot)$  and the MLP paramters  $\theta$  include the MLP weights  $\theta_w = W^1, \dots, W^{L+1}$  and the MLP bias  $\theta_b = b^1, \dots, b^{L+1}$ , and  $\hat{\mathbf{y}}$  is a estimated value. The pseudocode is presented in Algorithm 1 in subsection B in the appendix. We trained our MLP with approximately one million samples in a supervised learning setting. The network consists of two hidden layers with 256 and 128 units, respectively, each followed by Layer Normalization and GELU activation. The output layer maps to the target dimension directly. The loss function is the Smooth L1 loss. We used the Adam optimizer with an initial learning rate of  $3e^{-3}$ , and applied cosine annealing learning rate scheduling to improve convergence,  $T_{max} = 3000$ , and a minimum learning rate of  $1e^{-18}$ . The model was trained for 3000 epochs with a batch size of 1024. The training process resulted in convergence with a test loss of  $4.11e^{-3}$  and a training loss of  $3.01e^{-3}$ , and this close agreement implies acceptable generalization performance. On the validation PC, the average value of the cyclic integral with  $\delta\theta = 1e^{-7}$  in Eq. (13) decreased from 121.2ms to 29.5ms over one million iterations. Furthermore, the standard deviation of the computation time was reduced from 176ms to 11.3ms, indicating more stable and consistent computation.

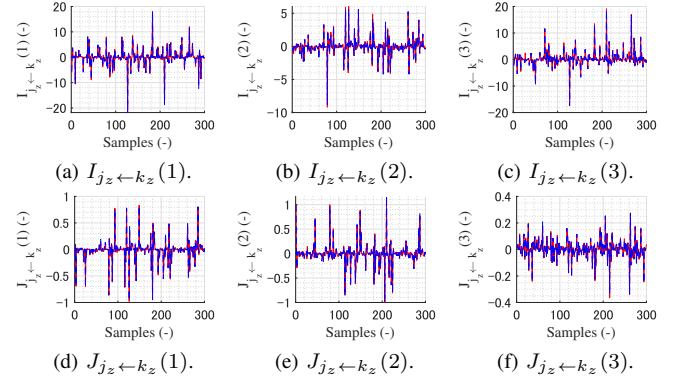


Fig. 6: The predictions of the circulant integration term in Eq. (13): The red solid line represents the ground-truth label data obtained from direct computation, while the blue dashed line indicates the values predicted by the MLP.

#### D. Experimental Validation

The designed experimental system consists of a microcontroller (ESP32-C6), two Time-of-Flight distance sensors (VL53L0X) for range measurements, and two current sensors (INA228iso). The actuation system employs two-axis electromagnetic coils wound with UL1007 AWG20 wire. Each coil has a diameter ranging from 16-18cm and a wire thickness of approximately 1cm, with 120 turns per coil. The maximum allowable current is 7A, based on a resistance of  $2\Omega$  and a 14V battery supply. To address size constraints, the coil along the axis perpendicular to the air-bearing platform is implemented using a ferromagnetic-core design and calibrated to produce an equivalent magnetic field in the horizontal plane. The basic 1D and 2D control experiments were conducted to enable simultaneous control, and the distance sensor measurements in Fig. 7 confirm the stable results around the target state.

## APPENDIX

### A. State Estimation on Experiment

We briefly notes the states estimation methods for readers' benefit. The estimations of their distance are executed periodically by the VL53L0X sensor. Let  $T_s$  be defined as the update period of command control values. As for the arbitrary distance at time  $t = kT_s$ , we obtain its approximated distance  $\bar{d}_{[kT_s]}$  by averaging previous  $N_s$  measurements:

$$\bar{d}_{[kT_s]} = \frac{1}{N_s} \sum_{n_s=1}^{N_s} d \left( (k-1)T_s + \frac{n_s-1}{N_s} T_s \right)$$

where  $d(t)$  is the distance measured by the sensor at time  $t$ . Here, the sensor on  $\{\mathcal{F}_L\}$  could measures the distances with the origin,  $d_{0 \leftarrow \mathcal{F}_L}$ , and MTQ  $\{\mathcal{F}_R\}$ ,  $d_{\mathcal{F}_R \leftarrow \mathcal{F}_L}$ . While the sensor on  $\{\mathcal{F}_R\}$  measures the distances with MTQ  $\{\mathcal{F}_L\}$ ,  $d_{\mathcal{F}_L \leftarrow \mathcal{F}_R}$ , and edge  $[0; 1.5; 0]$ ,  $d_{e \leftarrow \mathcal{F}_R}$ . To avoid the mutual interaction of distance measurement, we set  $d_{\mathcal{F}_L \leftarrow \mathcal{F}_R} = 0$ , that results the approximated distance between MTQ  $\{\mathcal{F}_{R,L}\}$  as  $\bar{d}_{RL[kT_s]} \approx \bar{d}_{\mathcal{F}_R \leftarrow \mathcal{F}_L[kT_s]}$ . Then,  $y_{L,R}(kT_s)$  are estimated from redundant sensor information to satisfy the distance

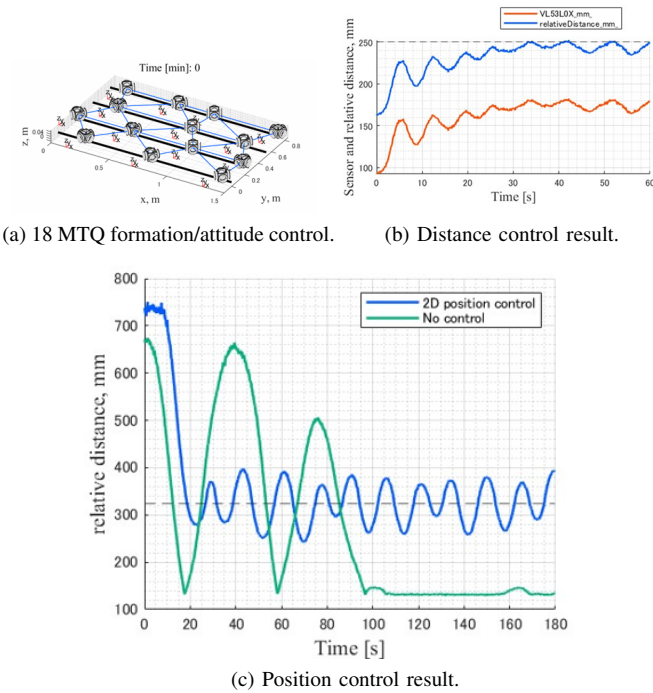


Fig. 7: Experimental results gained by Time-of-Flight ranging sensor VL53L0X: a) 18 MTQ control numerical simulation, b) Experimental distance control result for two MTQ on linear track, c) Experimental position control results for two MTQs: one on a linear air track and the other fixed on the ground.

constraint on the linear track:

$$y_L(kT_s) \approx \frac{\bar{d}_{0 \leftarrow \mathcal{F}_L[kT_s]} + (1.5 - y_{RL[kT_s]} - \bar{d}_{e \leftarrow \mathcal{F}_R[kT_s]})}{2},$$

$$y_R(kT_s) \approx \frac{(\bar{d}_{0 \leftarrow \mathcal{F}_L[kT_s]} + y_{RL[kT_s]}) + (1.5 - \bar{d}_{e \leftarrow \mathcal{F}_R[kT_s]})}{2}.$$

We derive the arbitrary  $y$ -axis relative velocity at time  $t = kT_s$  by the backward-Euler approximation and low-pass filter:

$$\frac{dy}{dt}(kT_s) = a \frac{dy}{dt}((k-1)T_s) + (1-a) \left[ \frac{y(kT_s) - y((k-1)T_s)}{T_s} \right]$$

where  $a \in [0, 1]$ . For this experiment, we select  $T_s = 0.1$ ,  $N_s = 7$ ,  $a = 0.97$ .

### B. Pseudocode of Coil Geometry Learning

We summarized the coil geometry learning presented in subsection III-C as the pseudocode in Algorithm 1.

### ACKNOWLEDGMENTS

The first author would like to thank Hayate Tajima at the University of Tokyo for valuable discussions and for providing code related to close-proximity satellite control. We also thank Yamato Hannya, Shunsuke Sato, Daisuke Wakao, and Atsushi Noda for their management and generous technical support.

### REFERENCES

- [1] S. Morioka, T. Inagawa, N. Homma, K. Murata, H. Yamaguchi, A. Shirane, M. Okada, K. Yasumoto, and

---

### Algorithm 1 Coil geometry learning in reference frame (A)

---

#### — Offline Phase —

- 1: **Inputs:** 1) index  $i \in [1, n_s]$ , 2) relative position  ${}^a r_{j \leftarrow k}^{(i)}$ , 3) unit vectors  ${}^a n_{j,k(x,y,z)}^{(i)}$  of the  $j, k$ th body-fixed frame
  - 2: **Outputs:** MLP weights  $\theta_w^*$ , MLP bias  $\theta_b^*$
  - 3: **for**  $i \in [1, \dots, n_s]$  **do**
  - 4:     Derive  $C^{A/B_{kz}} = [{}^a n_{k_x} {}^a n_{k_y} {}^a n_{k_z}]$  in Eq. (14)
  - 5:     Derive  $C^{D_{j \leftarrow kz}/B_{kz}} (C^{B_{kz}/A} {}^a r_{j \leftarrow k}^{(i)})$  in Eq. (15)
  - 6:     Stack inputs  $\mathbf{x}^{(f)} = [{}^a d_{j \leftarrow kz} r_{j \leftarrow k}^{(i)}, {}^a d_{j \leftarrow kz} n_{j_z}^{(i)}]^T$
  - 7:     Calculate  ${}^a I_{j_z \leftarrow k_z}$  and  ${}^a J_{j_z \leftarrow k_z}$  in Eq. (13)
  - 8:     Stack labels  $\mathbf{y}^{(f)} = [{}^a d_{j \leftarrow kz} I_{j_z \leftarrow k_z}; {}^a d_{j \leftarrow kz} J_{j_z \leftarrow k_z}]^T$
  - 9: **end for**
  - 10: Execute Eq. (16) to derive  $\theta_w^*, \theta_b^*$  by  $\mathbf{x}$  and  $\mathbf{y}$
- 
- #### — Online Phase —
- 11: **Inputs:** 1)  ${}^a r_{j \leftarrow k}$ , 2)  ${}^a n_{j,k(x,y,z)}$ , 3)  $\theta_w^*, \theta_b^*$
  - 12: **Outputs:** Near-field coefficient matrix  ${}^a Q_{j \leftarrow k} \in \mathbb{R}^{6 \times 9}$
  - 13: **for**  $l \in [x, y, z]$  **do**
  - 14:     Derive  $C^{A/B_{kl}} ({}^a n_{k(x,y,z)})$  in Eq. (14)
  - 15:     Derive  $C^{D_{j \leftarrow k_l}/B_{kl}} (C^{B_{kl}/A} {}^a r_{j \leftarrow k})$  in Eq. (15)
  - 16:     **for**  $m \in [x, y, z]$  **do**
  - 17:         Calculate  $[{}^a d_{j \leftarrow k_l} I_{j_m \leftarrow k_l}; {}^a d_{j \leftarrow k_l} J_{j_m \leftarrow k_l}]^T = f(x, \theta)$  in Eq. (13) where  $x = [{}^a d_{j \leftarrow k_l} r_{j \leftarrow k}; {}^a d_{j \leftarrow k_l} n_{j_m}]^T$
  - 18:         Calculate  $[{}^a I_{j_m \leftarrow k_l}; {}^a J_{j_m \leftarrow k_l}]^T$
  - 19:     **end for**
  - 20:     Stack  ${}^a K_{j \leftarrow k_l} = [{}^a K_{j_x \leftarrow k_l}, {}^a K_{j_y \leftarrow k_l}, {}^a K_{j_z \leftarrow k_l}] \in \mathbb{R}^{3 \times 3}$  for  $K = \{I, J\}$
  - 21: **end for**
  - 22: Stack  ${}^a Q_{j \leftarrow k} = \begin{bmatrix} {}^a I_{j \leftarrow k_x} & {}^a I_{j \leftarrow k_y} & {}^a I_{j \leftarrow k_z} \\ {}^a J_{j \leftarrow k_x} & {}^a J_{j \leftarrow k_y} & {}^a J_{j \leftarrow k_z} \end{bmatrix} \in \mathbb{R}^{6 \times 9} = 0$
- 

M. Kim, “Dense formation flying of multiple picosats for communication satellites and its technical challenges,” *IEICE Technical Report; IEICE Tech. Rep.*, vol. 124, no. 289, pp. 49–54, 2024.

- [2] S. Shim, Y. Takahashi, N. Usami, M. Kubota, and S.-i. Sakai, “Feasibility analysis of distributed space antennas using electromagnetic formation flight,” in *2025 IEEE Aerospace Conference*, 2025.
- [3] Y. Takahashi, S. Shim, and S.-i. Sakai, “Distance-based relative orbital transition for palm-sized satellite swarm with guaranteed escape-avoidance,” in *AIAA Scitech 2025 Forum*, 2025, p. 2068.
- [4] D. W. Kwon, R. J. Sedwick, S.-i. Lee, and J. L. Ramirez-Riberos, “Electromagnetic formation flight testbed using superconducting coils,” *Journal of Spacecraft and Rockets*, vol. 48, no. 1, pp. 124–134, 2011.
- [5] A. K. Porter, D. J. Alinger, R. J. Sedwick, J. Merk, R. A. Opperman, A. Buck, G. Eslinger, P. Fisher, D. W. Miller, and E. Bou, “Demonstration of electromagnetic formation flight and wireless power transfer,” *Journal of Spacecraft and Rockets*, vol. 51, no. 6, pp. 1914–1923, 2014.
- [6] S.-i. Sakai, R. Kaneda, K. Maeda, T. Saitoh, H. Saito, and T. Hashimoto, “Electromagnetic formation flight

- for leo satellites,” in *3rd International Symposium on Formation Flying, Missions and Technologies*, 2008.
- [7] R. C. Youngquist, M. A. Nurge, and S. O. Starr, “Alternating magnetic field forces for satellite formation flying,” *Acta Astronautica*, vol. 84, pp. 197–205, 2013.
- [8] M. A. Nurge, R. C. Youngquist, and S. O. Starr, “A satellite formation flying approach providing both positioning and tracking,” *Acta Astronautica*, vol. 122, pp. 1–9, 2016.
- [9] A. Sunny, “Single-degree-of-freedom experiments demonstrating electromagnetic formation flying for small satellite swarms using piecewise-sinusoidal controls,” Master’s thesis, University of Kentucky Libraries, 2019.
- [10] J. L. Ramirez Riberos, “New decentralized algorithms for spacecraft formation control based on a cyclic approach,” Ph.D. dissertation, Massachusetts Institute of Technology, 2010.
- [11] U. Ahsun, “Dynamics and control of electromagnetic satellite formations,” Ph.D. dissertation, Massachusetts Institute of Technology, Aeronautics and Astronautics Department, 2007.
- [12] L. M. Elias, D. W. Kwon, R. J. Sedwick, and D. W. Miller, “Electromagnetic formation flight dynamics including reaction wheel gyroscopic stiffening effects,” *Journal of Guidance, Control, and Dynamics*, vol. 30, no. 2, pp. 499–511, 2007.
- [13] A. Sakaguchi, “Micro-electromagnetic formation flight of satellite systems,” Ph.D. dissertation, Massachusetts Institute of Technology, 2005.
- [14] S. A. Schweighart, “Electromagnetic formation flight dipole solution planning,” Ph.D. dissertation, Massachusetts Institute of Technology, 2005.
- [15] L. Fan, M. Hu, and M. Yang, “Rotational and relative translational control for satellite electromagnetic formation flying in low earth orbit,” *Aircraft Engineering and Aerospace Technology*, vol. 89, no. 6, pp. 815–825, 2017.
- [16] E. Fabacher, S. Lizy-Destrez, D. Alazard, F. Ankersen, and A. Profizi, “Guidance of magnetic space tug,” *Advances in Space Research*, vol. 60, no. 1, pp. 14–27, 2017. [Online]. Available: <https://www.sciencedirect.com/science/article/pii/S0273117717302478>
- [17] A. Ayyad, “Optimal guidance and control for electromagnetic formation flying,” Master’s thesis, The University of Tokyo, 2019.
- [18] X.-l. Huang, C. Zhang, and X.-j. Ban, “Dipole solution and angular-momentum minimization for two-satellite electromagnetic formation flight,” *Acta Astronautica*, vol. 119, pp. 79–86, 2016.
- [19] R. W. Brockett, “Asymptotic stability and feedback stabilization,” *Differential Geometric Control Theory*, vol. 27, no. 1, pp. 181–191, 1983.
- [20] Y. Takahashi, H. Sakamoto, and S.-i. Sakai, “Control law of electromagnetic formation flight utilizing conservation of angular momentum: Time-varying control without using additional attitude actuator,” in *The 30th Workshop on JAXA Astrodynamics and Flight Mechanics*. Japan Aerospace Exploration Agency / Institute of Space and Astronautical Science, 2020.
- [21] R. Kaneda, S.-I. Sakai, T. Hashimoto, and H. Saito, “The relative position control in formation flying satellites using super-conducting magnets,” *Japan Society of Aeronautical Space Sciences*, vol. 56, no. 652, pp. 203–210, 2008.
- [22] C. Zhang and X.-L. Huang, “Angular-momentum management of electromagnetic formation flight using alternating magnetic fields,” *Journal of Guidance, Control, and Dynamics*, vol. 39, no. 6, pp. 1292–1302, 2016.
- [23] Z. Abbasi, J. B. Hoagg, and T. M. Seigler, “Decentralized electromagnetic formation flight using alternating magnetic field forces,” *IEEE Transactions on Control Systems Technology*, vol. 30, no. 6, pp. 2480–2489, 2022.
- [24] Y. Takahashi, H. Sakamoto, and S.-i. Sakai, “Simultaneous control of relative position and absolute attitude for electromagnetic spacecraft swarm,” in *AIAA Scitech 2021 Forum*, 2021, p. 1104.
- [25] Y. Takahashi, “Neural power-optimal magnetorquer solution for multi-agent formation and attitude control,” *arXiv preprint arXiv:2412.00548*, 2024.
- [26] H. J. Sussmann, “A general theorem on local controllability,” *SIAM Journal on Control and Optimization*, vol. 25, no. 1, pp. 158–194, 1987.
- [27] J.-M. Coron, “On the stabilization in finite time of locally controllable systems by means of continuous time-varying feedback laws,” *SIAM Journal on Control and Optimization*, vol. 33, no. 3, pp. 804–833, 1995.
- [28] H. J. Sussmann, “Subanalytic sets and feedback control,” *Journal of Differential Equations*, vol. 31, pp. 31–52, 1979.
- [29] H. Tajima, Y. Takahashi, T. Shibata, H. Sakamoto, and S.-i. Sakai, “Study on short range formation flight and docking control using ac magnetic field,” in *74th International Astronautical Congress, Baku, Azerbaijan*, 2–6 October 2023.
- [30] Y. Takahashi, H. Sakamoto, and S.-i. Sakai, “Kinematics control of electromagnetic formation flight using angular-momentum conservation constraint,” *Journal of Guidance, Control, and Dynamics*, vol. 45, no. 2, pp. 280–295, 2022.
- [31] A. Morgan, *Solving Polynomial Systems Using Continuation for Engineering and Scientific Problems*. SIAM, 2009.
- [32] W. Fehse, *Automated Rendezvous and Docking of Spacecraft*. Cambridge University Press, 2003, vol. 16.
- [33] S. A. Schweighart and R. J. Sedwick, “High-fidelity linhigh-fidelity linearized  $j_2$  model for satellite formation flight,” *Journal of Guidance, Control, and Dynamics*, vol. 25, no. 6, pp. 1073–1080, 2002.